CrossMark
click for updates

Hydrothermal synthesis of TiO₂ nanoparticles doped with trace amounts of strontium, and their application as working electrodes for dye sensitized solar cells: tunable electrical properties & enhanced photo-conversion performance†

Hadja Fatima Mehnane, Changlei Wang, Kiran Kumar Kondamareddy, Wenjing Yu, Weiwei Sun, Haimin Liu, Sihang Bai, Wei Liu,* Shishang Guo* and Xing-Zhong Zhao*

Strontium (Sr) doped TiO₂ nanoparticles are investigated with a view to studying the performance parameters of dye sensitized solar cells (DSSCs). Sr is used in trace levels (parts per million, ppm hereafter). The Sr doped TiO₂ and undoped TiO₂ nanoparticles are synthesized by the hydrothermal method and thin films of TiO₂ electrodes are prepared using these particles (average grain size of 24 nm). The electrodes are characterized by X-ray diffraction (XRD), Scanning Electron Microscopy (SEM), surface area (BET) and UV-vis absorption spectrometry. DSSCs are fabricated using the doped and undoped TiO₂ nanoparticle photoanodes. Their photovoltaic characteristics are studied by employing J–V measurements and electrochemical impedance spectroscopy (EIS). XRD studies reveal that the doping of Sr into the TiO₂ lattice slightly inhibits the growth of the particles and causes lattice distortions. The optical studies indicate a reduction in band-gap upon doping of TiO₂ films and a simultaneous enhancement in the photocurrent density (J_{sc}) and the photovoltage (V_{oc}). The photoanode doped with 50 ppm Sr exhibits the highest power conversion efficiency (PCE) of about 7.88% which is 12.73% higher than that of undoped TiO₂ cells. The effect of the Sr dopant on electron transport is studied by using EIS measurements. An improvement in electron life time is observed on the doping of TiO₂.
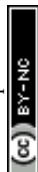
1. Introduction

Low cost solar power harvesting on a massive scale is a challenge which has led to the development of new photovoltaic technologies that pave the way for affordable renewable energy. One of the leading solar cell candidates is the dye sensitized solar cell (DSSC).[1–3] DSSCs based on nanocrystalline TiO₂ photoanodes have been regarded as one of the most promising alternatives to conventional solar cells due to their low cost, ease of fabrication, environmentally friendly nature and flexibility of design in view of their colors and transparencies and relatively high power conversion efficiencies (PCEs). These features make DSSCs the ideal photovoltaic devices for commercial applications,[4,5] and extensive research has been devoted to the development of high performance DSSCs.[6] The usage of a mesoporous TiO₂ n-type semiconductor electrode in DSSCs as a photoanode of high internal surface area has led to

School of Physics and Technology, Key Laboratory of Artificial Micro/Nano Structures of Ministry of Education, Wuhan University, Wuhan 430072, China. E-mail: xzzhao@ whu.edu.cn; gssyhx@whu.edu.cn; wliu@whu.edu.cn

† Electronic supplementary information (ESI) available. See DOI: 10.1039/c6ra26012h

a step change in the fields of photoelectrochemistry and photovoltaics. For state-of-the-art DSSCs, the architecture of the mesoporous TiO₂ electrode in the devices has seen much improvement since 1991, in terms of light absorption, light scattering, charge transport, suppression of charge recombination and alteration of the interfacial energetics.[5] TiO₂ is still the most successfully used wide band gap oxide material among other wide band semiconductor oxides such as ZnO, SnO₂, Nb₂O₅ and SrTiO₃, due to its stability, non-toxicity and highly refractive nature.[7] Therefore the development of advanced photovoltaic anode materials that effectively utilize solar energy from the visible region is an appealing challenge, particularly for DSSC applications, as the light absorption and charge collection take place at the dye sensitized mesoporous photoanode.[8,9] One of the effective ways to tailor the electronic properties of TiO₂ photoanodes is by deliberately inserting impurities into the TiO₂ lattice.[10] Such doping is also important in improving the performance of other kinds of mesoscopic solar cells.[11,12] Doping of DSCCs with TiO₂ is expected to control the morphology of the TiO₂ with the prospect of maximizing both the dye/TiO₂ interface area and the light absorption.[13,14]

Metallic[15–17] and non-metallic elements[18,19] are used in doping of TiO₂ photoanodes. Doping by rare earth and

transition metal ions, in particular, are reported by many researchers. However, studies on alkaline earth metal ion doped TiO_2 nanoparticles for DSSC photoanode applications, and investigations on their photovoltaic properties have rarely been carried out. The alkaline earth metals are interesting cationic dopants as they might donate s electrons from their outer shells when they are introduced into TiO_2 nanocrystals.[12] Peng et al.[20] reported that the substitution of Mg^{2+} ions into the anatase lattice affected its band edge movement and charge recombination and improved the open circuit voltage (V_{oc}) of DSSCs. Liu et al.[21] demonstrated that Ca doped TiO_2 photoanodes showed a positive shift in flat band potential of TiO_2 which caused an increase in efficiency of electron injection and improved electron transport properties. Sr doped TiO_2 electrodes of nanotube arrays were fabricated to improve the photo-conversion efficiency for water splitting applications.[22] Sr doped TiO_2 nanoparticles have been employed as photocatalysts where they showed enhanced photocatalytic activity due to their high surface area, improved charge transfer rate at the solid–liquid interface and suppression of electron–hole pair recombination.[23] DSSCs based on TiO_2 nanotube arrays that had been surface treated by strontium oxide (SrO) showed a higher photovoltaic performance.[24] However, a study of TiO_2 nanoparticles doped with the alkaline earth element Sr at ppm level concentrations for photoanodes of DSSCs has not previously been reported. Therefore the present investigations are aimed at employing a Sr doped TiO_2 photoanode and studying its influence on the photovoltaic performance of DSSCs. For the first time, the authors report on TiO_2 nanoparticles doped with trace amounts (several parts per million (ppm)) of Sr for DSSC applications. The photoanodes were prepared by the hydrothermal method and characterized by X-ray diffraction (XRD), scanning electron microscopy (SEM), and UV-visible absorption spectrometry. The influence of the dopant Sr on the electron transport and recombination processes in the photoanode is monitored by J–V characterisation studies and electrochemical impedance spectroscopy (EIS) measurements. It is found that doping with trace amounts of Sr is effective in enhancing the short circuit current density (J_{sc}) and V_{oc} simultaneously which contribute to a significant improvement in the conversion efficiency for DSSCs.

2. Experimental section

2.1. Materials

Titanium isopropoxide (TTIP, $Ti[OCH(CH_3)_2]_4$) and strontium nitrate ($Sr(NO_3)_2 \cdot 9H_2O$) were used as precursors of Ti and Sr respectively. In order to set the concentration of the solutions, following the earlier report,[25] two kinds of ethyl cellulose were employed to prepare an ethanolic mixture. Fluorine doped SnO_2 conductive glass (FTO, sheet resistance 10–15 U sq.$^{-1}$; Asahi Glass, Japan), N719 dye (Solaronix, Switzerland), iodine (12, 99.8%; Beijing Yili chemicals, China); lithium iodide (LiI, 99%), guanidine thiocyanate (GNCS) and 4-tert-butylpyridine (TBP) (Acros); and propylene carbonate (PC; Sinopharm Chemical Reagent Corporation, China) were used as received without any modifications.

2.2. Synthesis of TiO_2 and Sr doped TiO_2 paste

The pure and Sr doped TiO_2 pastes were prepared using the hydrothermal method as described elsewhere.[18] In a typical synthesis process, 2.1 g of acetic acid was dispersed into 10 ml of titanium isopropoxide (TTIP) using ultrasonic mixing for 10 min and the dispersion was then quickly dropped into 50 ml of deionized water under stirring to start the hydrolysis reaction. After 1 hour, Sr precursors of various trace concentrations (molar ratios: 20 ppm, 50 ppm, 80 ppm) were added to TTIP hydrolyzed solutions to prepare doped TiO_2 samples (and an undoped TiO_2 sample was also prepared). The hydrolysis was continued under vigorous stirring for 3 h at room temperature. Then 0.68 ml of nitric acid was added to each resultant precursor solution under continuous stirring. The temperature was maintained at a constant 80 °C for 4 h to obtain transparent solutions which were then filtered to wipe off insoluble impurities. The volume of each solution was adjusted to 68 ml by adding deionized water and each sample was then heated at 220 °C in a 100 ml autoclave for 12 h. After the hydrothermal process 0.4 ml of nitric acid was added to each sol–gel and it was stirred for 5 h. Finally each sol–gel was dispersed ultrasonically. In order to get final pure and Sr doped TiO_2 nanoparticles, the dispersed sol–gels were centrifuged and then dispersed in ethanol, ethyl cellulose and terpineol successively after proper drying. The mixtures were pulverized in an agate vial using a ball mill (QM-3SP2) for 12 h and sonicated for 30 min. These steps were alternately repeated three times in order to obtain homogenous solutions. During the pulverization, a plastic deformation of the TiO_2 crystal lattice took place which resulted in stresses and strains that distorted the lattice and formed many defects in the TiO_2 particles. Furthermore, the high surface energy and lattice distortion energy facilitated the achievement of the required activation energy for atomic and ionic diffusion at room temperature. The collisions that occurred among the grains of powder and the balls of the mixer mill caused a rise in interface temperature which induced the homogeneous incorporation of dopants. After the pulverization, ethanol was removed from the mixtures using rotary evaporation to extract the final pastes of pure and Sr doped TiO_2.

2.3. Preparation of the photoelectrodes and different DSSC devices

Films of uniform thickness were obtained by coating the pure and Sr doped TiO_2 pastes onto the FTO using the doctor-blade method. The films were dried on a hotplate at 125 °C and then sintered for 30 min at 500 °C in an oven to obtain the mesoporous electrodes. A TiO_2 scattering layer[26] was added to each electrode using the doctor blade method, and this was followed by annealing at 500 °C for 30 min. The pre-heated (125 °C for 30 min) mesoporous electrodes were then immersed in 0.5 mM ethanolic N719 solution at room temperature for 24 h and were washed with ethanol to remove the excess dye molecules. After ensuring that the nanocrystalline TiO_2 electrodes were covered by a monolayer of dye molecules, the electrodes were dried at 60 °C in air. Finally DSSCs were fabricated by sandwiching the electrolyte[27] layer between a N719

dye-loaded photoelectrode and Pt-coated FTO counter electrode. The Pt counter electrode was prepared by the sputtering method while the liquid electrolyte solution was prepared by dissolving 0.05 M LiI (lithium iodide, 99%), 0.03 M I_2 (iodine, 99.8%), 0.01 M PMII (1-methyl-3-propyl imidazolium iodide), 0.1 M GNCS (guanidine thiocyanate) and 0.5 M TBP (4-*tert*-butylpyridine) into a solvent composed of acetonitrile and PC (volume ratio: 1 : 4).

2.4. Characterization of DSSCs

The actual concentrations of Sr dopant were measured using inductively coupled plasma atomic emission spectroscopy (ICP-AES) [ESI, Table 1†] which confirmed that the concentrations were in the ppm range, albeit at lower levels than had been added to the precursor solutions. The structural analysis of the pure and Sr doped TiO_2 photoanodes was carried out by XRD studies, SEM and UV-vis spectroscopy. XRD patterns of the photoanodes were recorded using a Bruker XRD system (D8 Advanced, Germany) employing Cu Kα radiation. The morphology of the samples was monitored by field emission (FE)-SEM (Sirion, FEG). Specific surface area, pore volume, and pore size diameter were measured using nitrogen adsorption–desorption isotherms at 77 K obtained using a JW-BK122W analyzer (China). The optical absorption spectra were taken in the range of 300–800 nm using UV-vis spectrophotometry (Lambda 650S PerkinElmer). The amounts of dye loaded on the photoanodes were measured from the UV-vis spectra of the dye desorbed from the as prepared photoanodes upon immersion in an aqueous solution of NaOH (0.1 M). X-ray photoelectron spectroscopy (XPS) was carried out on a Thermo Fisher ESCA-LAB 250Xi, employing monochromatic Al Kα radiation (1486.68 eV), an ultrahigh vacuum under CAE mode with a pass energy of 20 eV and a step size of 0.05 eV. The binding energies were calibrated with respect to the carbon (C1s) peak (284.8 eV). Photovoltaic measurements of the devices were performed using a solar simulator CHI660C electrochemical workstation (CH Instruments, Shanghai, China), which provides AM 1.5 G illumination with an equivalent light intensity of 1000 W m^{-2} (under 1 Sun illumination) at room temperature. The irradiated area of each cell was confined to 0.25 cm^2 by using a light tight metal mask.

3. Results and discussion

XRD patterns of the Sr doped and undoped TiO_2 films are shown in Fig. 1. The well resolved sharp peaks indicate that the samples are crystallized into the anatase phase which was stable even after doping, implying that the doping with Sr has no effect on the phase structure of TiO_2. Kumaresan et al.[23] have reported similar results in which Sr did not promote an anatase to rutile transformation. The average crystallite size of the crystalline anatase was calculated by the Scherrer equation:[28]

$$d = \frac{k\lambda}{B \cos \theta} \tag{1}$$

where d is the crystallite size, k is a dimensionless shape factor which has a typical value of about 0.9, λ is the X-ray wavelength
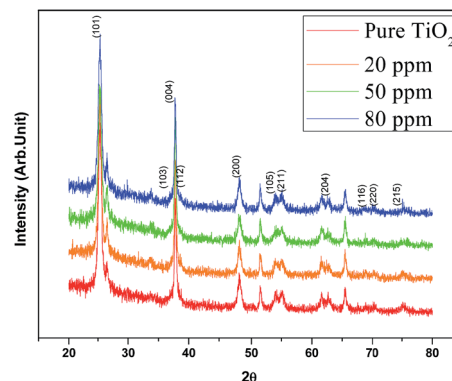

Fig. 1 XRD patterns of the synthesized TiO_2 and Sr doped TiO_2 photoanodes.

of Cu ($\sim$1.5406 Å), θ is the Bragg angle corresponding to the anatase (101) peak, and B is the line broadening at half the maximum intensity (FWHM). The average crystallite size of TiO_2 decreased with increasing concentration of Sr from 25.32 nm (undoped TiO_2) to 24.19 nm (50 ppm Sr doped TiO_2); the Sr dopant causes broadening of the (101) peak. According to Scherrer's formula, peak broadening is essentially associated with crystallite size and non-uniform strain (microstrain) due to shifts of atoms from their ideal position, which suggests that the dopant Sr distorts the TiO_2 lattice.[29] This may be attributed to the mismatch of the sizes of the dopant Sr^{2+} ion and host Ti^{4+} ions. The ionic radius of Sr^{2+} (1.18 Å) is higher than that of Ti^{4+} (0.60 Å) and so the insertion of larger ions into the lattice of smaller ions may enhance the possibility of local lattice distortions.[23] The reduction in average crystallite size with increasing concentration of Sr dopant has also been reported by A. Bakhshayesh et al.[30] Hamedani et al.[29] have reported that Sr^{2+} enters the TiO_2 lattice either in the interstitial sites or as a substitution for Ti^{4+}. The existence of larger sized Sr^{2+} in substitutional sites can cause volume compensating oxygen vacancies; such defect clusters would occur along different [hkl] directions in the TiO_2 lattice resulting in an alteration of the atomic distances[31] and leading to distortion of the structure. Long et al.[32] reported that the insertion of foreign atoms changes the crystallization degree of anatase and the number of oxygen vacancies (crystal defects) due to the difference in chemical states and ionic radii between the Ti host and the
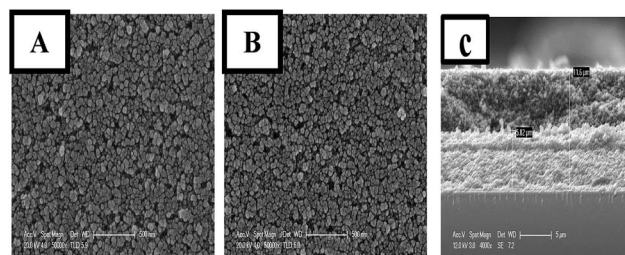

Fig. 2 SEM images displaying the surface morphologies of undoped photoanode (A) and the Sr doped TiO_2 photoanode (B); SEM image showing the cross section morphology of the films (C).
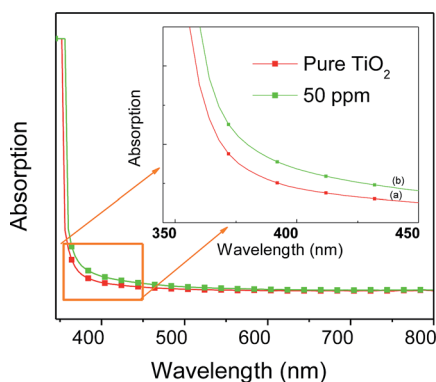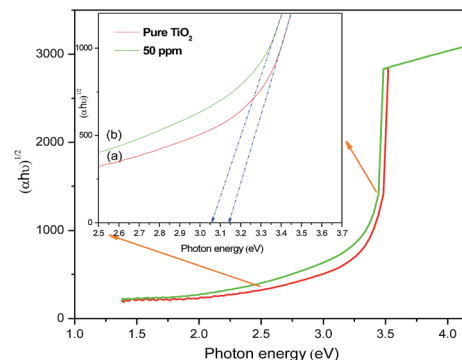
Table 1 Specific surface area, pore volume, and pore size diameters of TiO₂ nanoparticles and Sr doped TiO₂ nanoparticles

Sample ppm	Specific surface area m² g⁻¹	Pore volume cm³ g⁻¹	Pore size diameter nm
0	77.13	0.537	16.237
20	82.66	0.726	16.616
50	77.10	0.819	24.733
80	61.46	0.559	22.430

Fig. 4 Plots of $(\alpha h\nu)^{1/2}$ vs. photon energy of (a) pure TiO₂ and (b) Sr (50 ppm) doped TiO₂ photoanodes.

doping guest. The XRD peaks corresponding to the Sr dopant are not observed which may be due to its low doping concentration.

The surface morphologies of the pure and Sr doped (50 ppm) TiO₂ films are illustrated in Fig. 2(A) and (B), respectively. The morphology of both samples is highly crystalline which is in good agreement with the XRD results. It can also be seen from the SEM images that the photoelectrodes have typical porous structures. The average size of the nanoparticles is in the range of 20–30 nm. The cross section morphology of the films is provided in Fig. 2(c). The thickness of the films measured from SEM images is found to be around (12 μm ± 0.5).

The results of BET specific surface area values for doped and undoped samples are listed in Table 1. All the samples possess quite high specific surface area values, ranging from about 60 to 80 m² g⁻¹. The mean pore size diameter calculated by the BJH method is around 16–24 nm for all of the samples. A clear correlation exists among the various morphological parameters. The Sr doped TiO₂ photoanodes display higher pore size diameters, which increase up to 50 ppm of dopant, indicating that the doped samples may be more efficient compared to the undoped one with respect to dye loading. Additionally the measurements of pore size diameter show that 50 ppm doped samples have the most uniform structure, which might be attributed to their porous morphology. These parameters can influence the absorption capability of the photoanodes. Fig. 3 shows the UV-visible absorption spectra of undoped and Sr doped TiO₂ films. The absorption curve of Sr doped (50 ppm) TiO₂ film is red shifted relative to the undoped TiO₂ film. The red shift of the absorption edge suggests a reduction of the

energy band gap. The Tauc model[33] was employed to determine the optical band gap energy using the following equation:

$$\alpha h\nu = A(h\nu - E_g)^r \quad (2)$$

where $h\nu$ is the photon energy, E_g is the optical band gap, A is a constant, r is equal to 2 for allowed indirect optical transitions and α is the absorption coefficient. The measured indirect band gaps of the undoped and Sr (50 ppm) doped TiO₂ samples (Fig. 4) are 3.14 eV and 3.05 eV respectively. The reduction in the band gap can be attributed to the insertion of Sr into the TiO₂ lattice. Since the lower edge of the CB is made up of Ti⁴⁺ 3d bands, the substitution of Ti⁴⁺ with the Sr cation is expected to affect the CB structure. Bakhshayesh and Bakhshayesh[34] reported that the reduction in the energy band gap of strontium doped and co-doped TiO₂ nanoparticles is due to a modification of the conduction band. Naraginti et al.[35] also suggested that the effect of Sr on the electronic energy levels would be near to the conduction band edge causing an energy band gap reduction.

The adsorbed amount of dye for each film was determined by UV-vis absorption measurements. UV-vis absorption spectra of the desorbed dye from TiO₂ films measured in NaOH solution are shown in Fig. 5. It can be noted that the 50 ppm Sr doped TiO₂ film has the strongest dye absorption peak around 340–550 nm, indicating the higher dye loading in this film compared with that of the pure TiO₂, 20 ppm, and 80 ppm films. The variation in pore volume and pore size diameter can be directly

Fig. 3 UV-visible absorption spectra of (a) pure TiO₂ and (b) Sr (50 ppm) doped TiO₂ photoanodes.
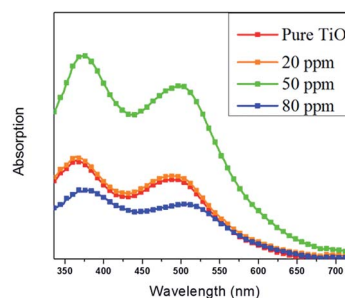
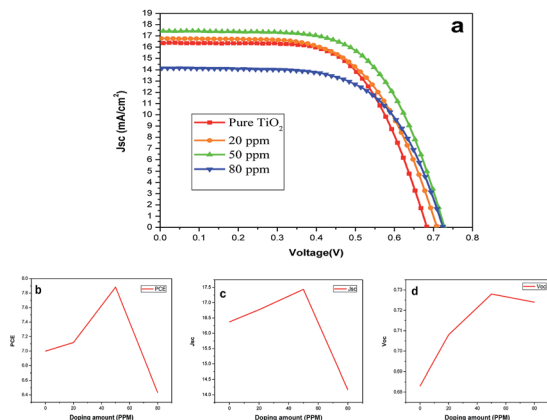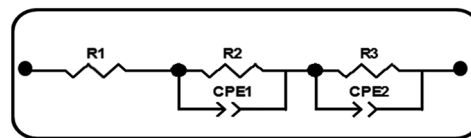Fig. 5 Absorption spectra of the dye N719 desorbed from the pure TiO₂ and Sr doped TiO₂ films.

Fig. 6 (a) J–V curve characteristics of DSSCs based on the undoped and Sr doped TiO$_2$ photoanodes under 1 Sun illumination; (b–d) variations of photovoltaic parameters of DSSCs for different doping amounts.

Scheme 1 Equivalent circuit model of DSSCs. R_1: serial resistance. R_2: charge-transfer resistance of the FTO/TiO$_2$ and counter electrode/electrolyte interfaces. CPE$_1$: constant phase element of the FTO/TiO$_2$ and counter electrode/electrolyte interfaces. R_3: electron transfer in TiO$_2$/dye/electrolyte interfaces. CPE$_2$: constant phase element of TiO$_2$/dye/electrolyte interfaces.

correlated to dye loading. The high dye loading exhibited by the 50 ppm Sr doped TiO$_2$ film can be attributed to its bigger pore volume and pore size.

XPS core level spectra of the undoped and doped TiO$_2$ nanoparticles for Sr are shown in the ESI [Fig. 1(a)–(e)].† It is difficult to find Sr in the Sr3d, Sr3s, and Sr3p regions as Sr is at ppm range. It is also difficult to identify the peaks corresponding to Sr4p and Sr4s from the regions of O2s and Ti3p as the peaks of Sr are superimposed by O and Ti peaks, respectively. However, it is found that peaks related to the O2s and Ti3p are shifted to higher binding energies with doping of up to 50 ppm Sr, and returned to lower binding energies for 80 ppm Sr which indicates an influence of the incorporated Sr dopant.

Fig. 6(a) represents the J–V characteristics of DSSCs of undoped and Sr doped TiO$_2$ photoanodes. The photovoltaic parameters including V_{oc}, J_{sc}, fill factor (FF), and PCE are listed in Table 2. Compared with the pure TiO$_2$, the Sr doped TiO$_2$ photoanodes showed better photovoltaic performances. A maximum PCE of 7.88% was obtained for the 50 ppm Sr doped TiO$_2$ based DSSC which is an improvement of 12.73% relative to that of the DSSC based on the pure TiO$_2$ photoanode. Fig. 6(b) shows the varying PCEs of the DSSCs of undoped and doped TiO$_2$ films. A significant improvement in the J_{sc} values was observed for DSSCs of TiO$_2$ nanoparticle electrodes doped with 20 or 50 ppm Sr. The J_{sc} of the DSSC is increased from 16.37 mA cm^{-2} (undoped TiO$_2$) to a maximum value of 17.43 mA cm^{-2} for the 50 ppm Sr doped TiO$_2$ cell (Fig. 6(c)). This enhancement in

J_{sc} is one of the reasons for improved efficiency.[36] Fig. 6(d) illustrates the variation of V_{oc} with different concentrations of dopant. The value of V_{oc} increased from 0.683 V for the pure TiO$_2$ cell to 0.728 V for the 50 ppm Sr doped cell, and then decreased to 0.724 V for the 80 ppm Sr doped cell. The simultaneous improvement of J_{sc} and V_{oc} values has been reported by many researchers.[24,30,34]

The improvement in J_{sc} is due to both the narrowed band gap of the 50 ppm Sr doped TiO$_2$ that facilitates the better photoexcitation of the semiconductor, and the increased dye absorption. The efficient photoexcitation of TiO$_2$ and enhanced photo-injection contributes to the higher electron density. Furthermore, the introduction of Sr^{2+} leads to the generation of oxygen vacancies, as expressed by the following equation:[37]

$$Sr^{2+} + TiO_2 \rightarrow Sr''_{Ti} + 2V_O^{\cdot\cdot}$$
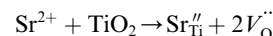
These oxygen vacancy lattice defects, resulting from the substitution of Sr^{2+} in the sites of Ti^{4+}, can trap photo-generated holes, elongating the life of the photo-excited electrons and holes and thereby increasing J_{sc}.[23,29,30,34] The life times of the photon excited charges were measured using EIS studies and are presented in the next section. The increase in V_{oc} for Sr doped TiO$_2$ samples up to 50 ppm is due to the enhancement in the number of electrons being injected and/or the suppression of recombination of injected electrons. The substitution of Ti^{4+} ions by Sr^{2+} leads to the distortion of TiO$_6$ octahedra and the introduction of oxygen vacancies thus generating dipole moments as well as internal polarization fields in the structure which facilitate the better charge separation efficiency of photo-generated electrons and holes[38] and decrease the recombination probability.[39] All of the above reasons are beneficial for a higher V_{oc}.

EIS was carried out in the frequency range of 0.1 to 10^5 Hz to investigate the effect of Sr doping on the charge transport

Table 2 Performance of DSSCs based on pure TiO$_2$ and Sr doped TiO$_2$ photoanodes

Doping amount (ppm)	J_{sc} (mA cm^{-2})	V_{oc} (V)	PCE (%)	FF (%)
0	16.37	0.683	6.99	0.62
20	16.77	0.708	7.11	0.59
50	17.43	0.728	7.88	0.62
80	14.16	0.724	6.43	0.62

Table 3 EIS parameters of the DSSCs determined by fitting the experimental data to the equivalent circuit model

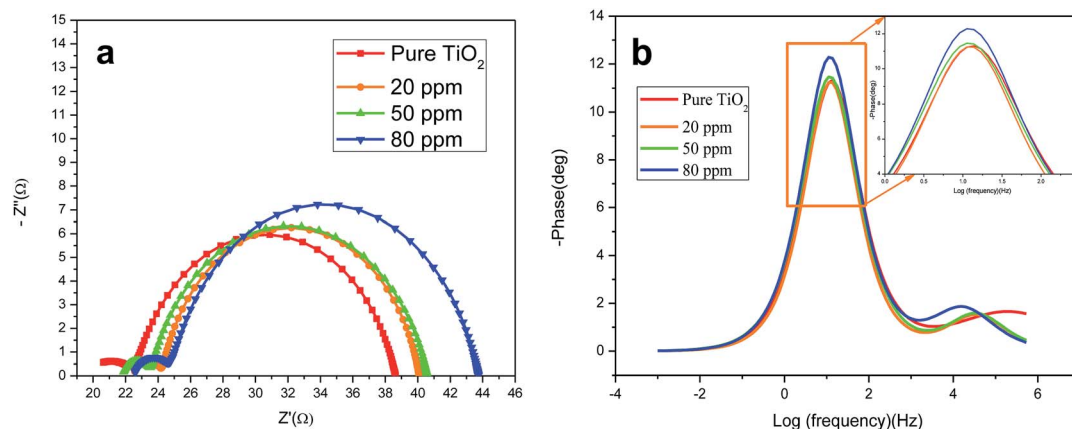| Electrodes (ppm)	R_1	R_2	R_3	f_{max}	τ_e (ms)
0	19.48	3.227	16.642	13.803	11.533
20	22.49	1.751	16.882	11.220	14.18
50	21.80	1.737	17.681	7.413	21.47
80	22.53	2.239	19.129	9.120	17.45

Fig. 7 (a) EIS of DSSCs based on the undoped and Sr doped TiO_2 photoanodes under 1 Sun illumination at the applied bias of V_{oc}; (b) Bode plots of DSSCs based on pure TiO_2 and TiO_2 doped with different amounts of Sr.

properties of the DSSCs. Based on the theoretical analysis of charge transport, the experimental data were fitted to the equivalent circuit model of the DSSCs which is given in Scheme 1. The EIS parameters of the DSSCs determined by fitting the experimental data to the equivalent circuit model are given in Table 3. EIS plots (Fig. 7(a)) of the cells of doped and undoped TiO_2 taken at the applied bias of V_{oc} under one Sun illumination contain two semicircles. The smaller semicircle in the high frequency region is attributed to the charge transfer resistance (R_2) at the two respective interfaces (electrolyte/Pt counter electrode) and (FTO/TiO_2) and the larger semicircle in the low frequency region is mainly related to the charge recombination resistance R_3 across the TiO_2/electrolyte interface with a partial contribution from electron transport and accumulation in TiO_2 photoanodes.[39]

The Nyquist plots show that the resistance related to electron recombination (R_3) increases with Sr content. The R_3 values are 16.642 Ω, 16.882 Ω, 17.681 Ω, 19.129 Ω for the undoped and 20 ppm Sr, 50 ppm Sr and 80 ppm Sr doped TiO_2 based cells, respectively. The higher values of R_3 indicate reduced electron recombination in Sr doped electrodes.[40] The life time (τ_e) of the photoelectrons is estimated using the relation:[41]

$$\tau_e = \frac{1}{2\pi f_{max}} \quad (3)$$

where f_{max} is the characteristic peak frequency value of the semicircle at lower frequency in the Bode plots (Fig. 7(b)). The electron life time increased with Sr doping up to 50 ppm. The measured life time of electrons for the undoped TiO_2 cell is 11.533 ms, and for 20 ppm Sr, 50 ppm Sr and 80 ppm Sr doped TiO_2 based cells, the life times are 14.18 ms, 21.47 ms and 17.45 ms respectively. These prolonged electron life times of doped TiO_2 nanoparticles indicate the suppression of the recombination rate and thus an increase in V_{oc}. This can be attributed to the reduction in the band gap as well as the lattice distortions that tend to accumulate variable oxygen vacancies so as to trap the photo-generated holes, extending the life of photo-excited electrons and holes[38] which results in better electron transport in the cells of doped TiO_2 particles. From the present

investigations we infer that the DSSC of 50 ppm Sr doped TiO_2 nanoparticles exhibit optimum performance which will be beneficial for future applications. With this knowledge it is expected that Sr doped TiO_2 mesoporous electrodes can also be employed for other organic photovoltaic cell applications.

4. Conclusions

The present work provides a characterization of the effect of dopant (at very low concentrations) on the structural and electronic properties of TiO_2 nanocrystalline photoanodes for DSSC applications, and describes significant improvements in the performance of DSSCs. XRD and SEM studies reveal the formation of lattice distortions and crystal defects introduced by Sr insertion. Moreover, Sr doping leads to a reduction in the energy band gap of TiO_2 which plays an essential role in enhancing the performance parameters of the devices. The dye adsorption is improved by doping as a consequence of increased pore volume and pore diameter. DSSCs fabricated using a series of Sr doped TiO_2 photoanodes, show an overall conversion efficiency of 7.88% at 50 ppm Sr doping, which is 12.73% higher than that of cells made of pure TiO_2. In addition, the values of J_{sc} and V_{oc} of Sr doped TiO_2 photoanodes increase simultaneously with increasing concentration of Sr dopant up to 50 ppm. Recombination of charges is effectively suppressed by doping TiO_2 with Sr. The highest electron life time is achieved for 50 ppm Sr doped TiO_2. Thus it is reasonable to infer that the Sr doped TiO_2 may be developed as a promising material for future photo-conversion energy devices.

Acknowledgements

Notes and references

1 M. Jørgensen, J. E. Carlé, R. R. Søndergaard, M. Lauritzen, N. A. Dagnæs-Hansen, S. L. Byskov, T. R. Andersen, T. T. Larsen-Olsen, A. P. Böttiger and B. Andreasen, *Sol. Energy Mater. Sol. Cells*, 2013, **119**, 84–93.

2 M. Graetzel, R. A. Janssen, D. B. Mitzi and E. H. Sargent, *Nature*, 2012, **488**, 304–312.

3 A. Hagfeldt, G. Boschloo, L. Sun, L. Kloo and H. Pettersson, *Chem. Rev.*, 2010, **110**, 6595–6663.

4 B. O'Regan and M. Grätzal, *Nature*, 1991, **353**, 737–740.

5 N. Tétreault and M. Grätzel, *Energy Environ. Sci.*, 2012, **5**, 8506–8516.

6 S. Mathew, A. Yella, P. Gao, R. Humphry-Baker, B. F. Curchod, N. Ashari-Astani, I. Tavernelli, U. Rothlisberger, M. K. Nazeeruddin and M. Grätzel, *Nat. Chem.*, 2014, **6**, 242–247.

7 X. Xu, S. Bai, Y. Fang, A. Chen, D. Li and Y. Lin, *Electrochim. Acta*, 2014, **145**, 286–290.

8 Y. J. Kim, M. H. Lee, H. J. Kim, G. Lim, Y. S. Choi, N. G. Park, K. Kim and W. I. Lee, *Adv. Mater.*, 2009, **21**, 3668.

9 J. Wu, Z. Lan, J. Lin, M. Huang, Y. Huang, L. Fan and G. Luo, *Chem. Rev.*, 2015, **115**, 2136–2173.

10 R. L. Hoye, K. P. Musselman and J. L. MacManus-Driscoll, *APL Mater.*, 2013, **1**, 060701.

11 F. Giordano, A. Abate, J. P. C. Baena, M. Saliba, T. Matsui, S. H. Im, S. M. Zakeeruddin, M. K. Nazeeruddin, A. Hagfeldt and M. Grätzel, *Nat. Commun.*, 2016, **7**, 10379.

12 B. Roose, S. Pathak and U. Steiner, *Chem. Soc. Rev.*, 2015, **44**, 8326–8349.

13 Z.-S. Wang, H. Kawauchi, T. Kashima and H. Arakawa, *Coord. Chem. Rev.*, 2004, **248**, 1381–1389.

14 X. Chen and S. S. Mao, *Chem. Rev.*, 2007, **107**, 2891–2957.

15 Y. Duan, N. Fu, Q. Liu, Y. Fang, X. Zhou, J. Zhang and Y. Lin, *J. Phys. Chem. C*, 2012, **116**, 8888–8893.

16 J. Zhang, W. Peng, Z. Chen, H. Chen and L. Han, *J. Phys. Chem. C*, 2012, **116**, 19182–19190.

17 J. J. Teh, S. L. Ting, K. C. Leong, J. Li and P. Chen, *ACS Appl. Mater. Interfaces*, 2013, **5**, 11377–11382.

18 Y. Xie, N. Huang, S. You, Y. Liu, B. Sebo, L. Liang, X. Fang, W. Liu, S. Guo and X.-Z. Zhao, *J. Power Sources*, 2013, **224**, 168–173.

19 T. Ma, M. Akiyama, E. Abe and I. Imai, *Nano Lett.*, 2005, **5**, 2543–2547.

20 T. Peng, K. Fan, D. Zhao and J. Chen, *J. Phys. Chem. C*, 2010, **114**, 22346–22351.

21 Q. Liu, Y. Zhou, M. Wang, X. Zhao and Y. Lin, *J. Alloys Compd.*, 2013, **548**, 161–165.

22 H. A. Hamedani, N. K. Allam, H. Garmestani and M. A. El-Sayed, *J. Phys. Chem. C*, 2011, **115**, 13480–13486.

23 L. Kumaresan, M. Mahalakshmi, M. Palanichamy and V. Murugesan, *Ind. Eng. Chem. Res.*, 2010, **49**, 1480–1485.

24 J.-G. Chen, C.-Y. Chen, C.-G. Wu, C.-Y. Lin, Y.-H. Lai, C.-C. Wang, H.-W. Chen, R. Vittal and K.-C. Ho, *J. Mater. Chem.*, 2010, **20**, 7201–7207.

25 S. Ito, T. N. Murakami, P. Comte, P. Liska, C. Grätzel, M. K. Nazeeruddin and M. Grätzel, *Thin Solid Films*, 2008, **516**, 4613–4619.

26 H. Liu, L. Liang, T. Peng, H. F. Mehnane, B. Sebo, S. Bai, Z. Yu, W. Yu, W. Liu and S. Guo, *ElectrochimicaActa*, 2014, **132**, 25–30.

27 S. Bai, L. Liang, C. Wang, H. F. Mehnane, C. Bu, S. You, Z. Yu, N. Cheng, H. Hu and W. Liu, *J. Power Sources*, 2015, **280**, 430–434.

28 R. van de Krol, A. Goossens and E. A. Meulenkamp, *J. Electrochem. Soc.*, 1999, **146**, 3150–3154.

29 H. A. Hamedani, N. K. Allam, M. A. El-Sayed, M. A. Khaleel, H. Garmestani and F. M. Alamgir, *Adv. Funct. Mater.*, 2014, **24**, 6783–6796.

30 A. Bakhshayesh and N. Bakhshayesh, *J. Colloid Interface Sci.*, 2015, **460**, 18–28.

31 T. j. Chen and P. Shen, *J. Phys. Chem. C*, 2008, **113**, 328.

32 L.-L. Long, A.-Y. Zhang, J. Yang, X. Zhang and H.-Q. Yu, *ACS Appl. Mater. Interfaces*, 2014, **6**, 16712–16720.

33 J. Tauc, *Amorphousand Liquid*, PlenumPress, London, NewYork, 1st edn, 1974.

34 A. Bakhshayesh and N. Bakhshayesh, *Mater. Sci. Semicond. Process.*, 2016, **41**, 92–101.

35 S. Naraginti, T. Thejaswini, D. Prabhakaran, A. Sivakumar, V. Satyanarayana and A. A. Prasad, *Spectrochim. Acta, Part A*, 2015, **149**, 571–579.

36 Q. Liu, *Electrochim. Acta*, 2014, **129**, 459–462.

37 W. Li, J. Yang, J. Zhang, S. Gao, Y. Luo and M. Liu, *Mater. Res. Bull.*, 2014, **57**, 177–183.

38 Y. J. Kim, M. H. Lee, H. J. Kim, G. Lim, Y. S. Choi, N. G. Park, K. Kim and W. I. Lee, *Adv. Mater.*, 2009, **21**, 3668–3673.

39 Z. Zhao and Q. Liu, *J. Phys. D: Appl. Phys.*, 2008, **41**, 085417.

40 W. Sun, X. Sun, T. Peng, Y. Liu, H. Zhu, S. Guo and X.-Z. Zhao, *J. Power Sources*, 2012, **201**, 402–407.

41 R. Kern, R. Sastrawan, J. Ferber, R. Stangl and J. Luther, *Electrochim. Acta*, 2002, **47**, 4213–4225.